4

Strain engineering of WS_2, WSSe and WSe_2 monolayers

4.1 Introduction

In layered 2D materials, the physical properties are changed by controlling the number of layers (Castro Neto, Guinea, Peres, Novoselov, & Geim, 2009). Moreover, the flexibility of 2D materials make them suitable for nanoelectronic device applications (X. L. Li et al., 2017). Alternatively, there are several methods, such as the external electric field, strain, and heterostructure used to design the appropriate optoelectronic properties (Johari & Shenoy, 2012). In graphene and 2D TMDs, the effect of external electric field is not obvious in monolayer, but it is more obvious in multilayer systems (Ramasubramaniam, Naveh, & Towe, 2011). The calculation of DFT shows that the change in bandgap and effective mass of TMDs by applying electric field and strain (Sharma, Kumar, Ahluwalia, & Pandey, 2014). In these heterostructures, the interaction between layers depends highly on the interlayer spacing. This is used as the design parameter to modify the properties of a TMDs based heterostructure (F. Wang et al., 2017). The strain is proposed as a value-added engineering parameter, which can modify the physical properties of TMDs significantly (He et al., 2016). For example, applying uniaxial and biaxial strain to TMDs led to semiconductor-metal transitions (Johari & Shenoy, 2012). The changes in electronic properties, such as bandgap, effective mass, and mobility of carriers, can be understood as the softening/hardening of phonons after applying compressive and tensile stresses (Amin, Kaloni, & Schwingenschlögl, 2014). Note that in TMDs heterostructures, the strain can be realized experimentally by changing the parameters of the substrate on which TMDs will be synthesized.

The inherent strain in Janus monolayer encouraged us for the study of the dynamic stability of TMDs based MX_2 single layer under biaxial tensile and compressive strain. In this study, we have considered WS_2 and WSe_2 as the parent monolayer and its derived WSSe monolayer. DFT calculations are performed to determine the dispersion of phonon modes. It is used to understand the stability of unstrained and strained monolayers. Compressive and tensile deformations are applied to realize maximum strain sustainable limit and its impact on the electronic properties of considered monolayers.

4.2 Computational Details

DFT calculations are carried out using the QE package (Giannozzi et al., 2009b; Kohn & Sham, 1965b). Plane-wave basis sets based pseudopotentials with GGA-PBE exchange-correlation potential is used throughout the calculation (Tasker, 1996). The GGA-PBE+SOC is also considered, which may have a significant impact on the electronic properties of unstrained and strained monolayers. The energy cutoff for the plane wave basis set is fixed at 50 Ryd. Broyden-Fletcher-Goldfarb-Shenno scheme (BFGS) method is used to optimize the structural parameters. The convergence criteria for force and energy were set at $5x10^{-3}$ eV/Å and 10^{-4}Ryd, respectively. To integrate the Brillouin zone (BZ) according to the Monkhorst-Pack scheme (Pack & Monkhorst, 1977), 12x12x1 K-point sampling is used for SCF and 24x24x1 for phonon dispersion and electronic properties. A vacuum of 25 Å is maintained in the c-axis to avoid the influence of the

interaction between the layers. The DFPT theory is used to calculate the dispersion of phonon bands along wave vector K (Baroni, De Gironcoli, Dal Corso, & Giannozzi, 2001).

4.3 Results and Discussion

The atoms are organized in triangular prismatic symmetry for WS_2 and WSe_2 monolayers and possess the D_{3h} symmetry. The Janus WSSe monolayer is built by exchanging top side of the S atom of WS_2 with Se atoms. Janus monolayer breaks the out-plane symmetry; that's why symmetry has reduced from D_{3h} to C_{3V}. In Janus monolayer, W atom has 6-fold symmetry, and S/Se atoms have 3-fold symmetry (Yin, Wen, Nie, Wei, & Liu, 2018). Figure 4.1 shows the optimized crystal structure of WS_2, WSe_2, and Janus WSSe monolayer and lattice parameters are 3.19 Å, 3.25 Å, and 3.34 Å, respectively, and in order with earlier reported (Cheng, Zhu, Tahir, & Schwingenschlögl, 2013; Kang, Tongay, Zhou, Li, & Wu, 2013). The optimized bond lengths and bond angles are listed in the corresponding optimized crystal structure and matched with the reported results (Chang & Fan, 2013). The change in structures can be attributed due to the different atomic radii.

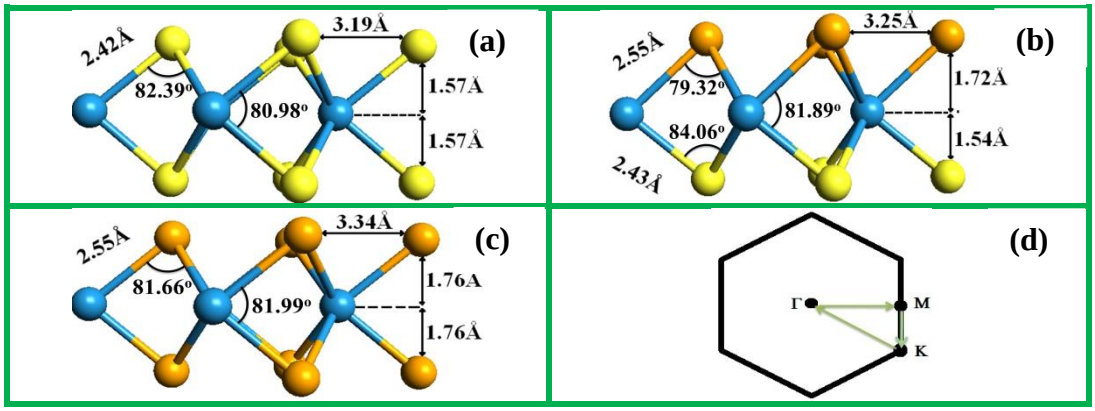

Figure 4.1 Optimized geometries and corresponding structural parameters of (a) WS2, (b) WSSe and (c) WSe_2 monolayer; (d) Schematic representation of hexagonal BZ.

4.3.1 Structural stability

The phonon band dispersion for considered monolayers is shown in Figure 4.3. The WS_2 and WSe_2 monolayers have three atoms in the unit cell; that's why phonon band dispersion has nine vibrational modes. These general vibration modes are shown in Figure 4.2 with corresponding vibration directions W and S (Se). The lowest three magnitude phonon modes marked with ZA, TA, and LA, which correspond to out-of-plane, transverse, and longitudinal acoustic modes, respectively. The LA and TA modes have a linear relationship with the wave vector, while the ZA mode has a quadratic relationship. The other six modes are optical phonon modes. Due to the different atomic mass of atoms in the unit lattice, their frequency is different from the acoustic mode. There are two non-polar (TO_1 and LO_1); two polar (TO_2 and LO_2) and the remaining two are homopolar modes (X. Zhang et al., 2015).

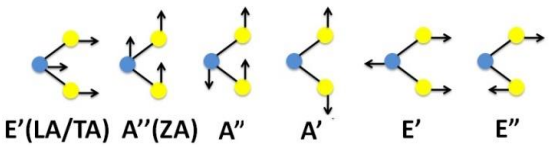

Figure 4.2 Schematic representation of vibrational modes of WS2 monolayer (W: blue, S: yellow).

All vibrational modes have a positive frequency, indicating the dynamic stability of these monolayers. The frequency difference between the optical and acoustic modes for WS_2, WSSe, and WSe_2 monolayer is about 109 cm^{-1}, 44 cm^{-1}, and 34 cm^{-1}, respectively. The softening in acoustic mode is observed from WS_2 to WSSe to WSe_2, and the optical frequency has decreased in the same order, indicating that the corresponding group speed has reduced. The obtained results are consistent with those previously reported in these monolayers (Amin et al., 2014; Cheng et al., 2013; Molina-Sánchez & Wirtz, 2011; W. Zhao et al., 2013).

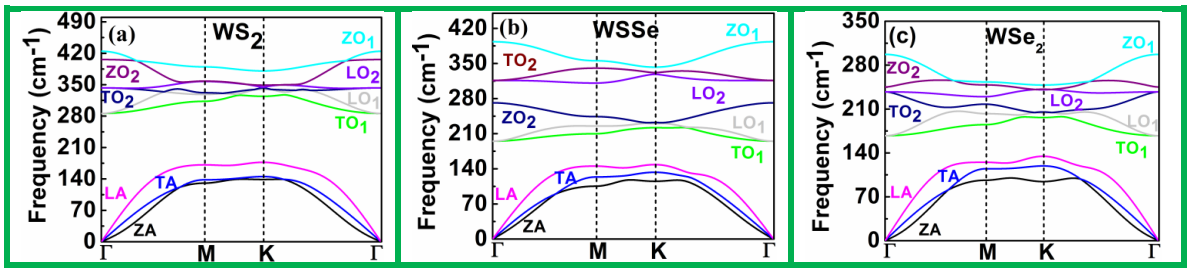

Figure 4.3phonon band dispersion of (a) WS_2, (b) WSSe, and (c) WSe_2 monolayers

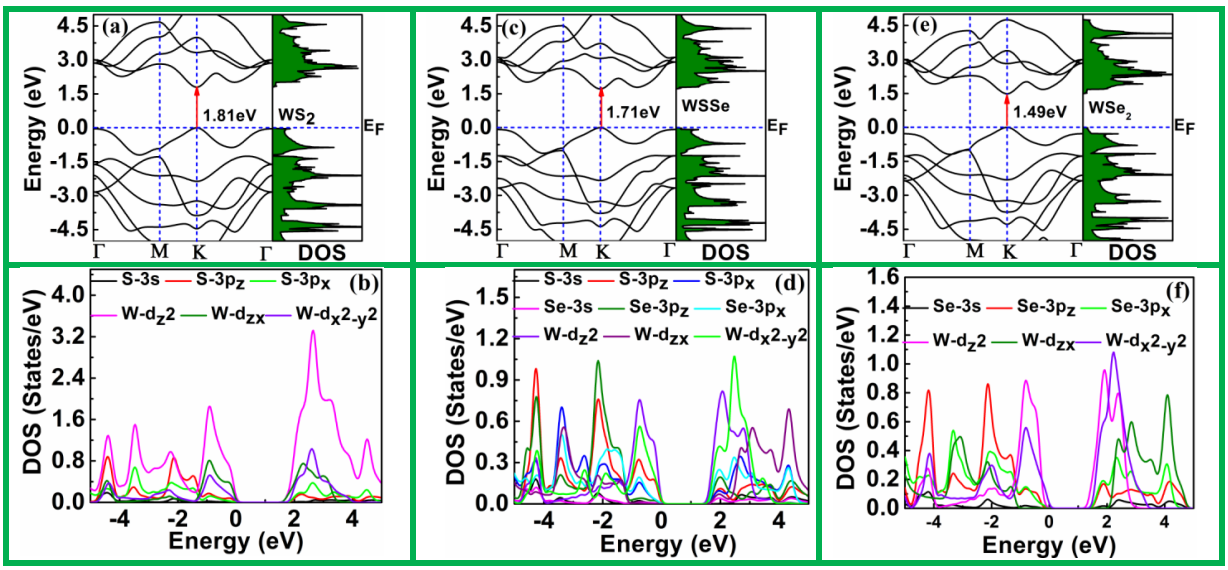

Figure 4.4 (a), (c) and (e) are the band structure and (b), (d) and (f) are the PDOS of WS_2, WSSe and WSe_2 monolayer, respectively.

4.3.2 Electronic properties

The band structures of considered monolayers are calculated in the range of -5 to 5 eV, shown in Figure 4.4. The direct bandgap 1.81 eV (1.54 eV), 1.71 eV (1.44eV), and 1.49 eV (1.20eV) observed using GGA-PBE (GGA-PBE+SOC) at the K point of BZ for WS_2, WSSe and WSe_2 monolayers, respectively. The bandgap values are consistent with literature (Cheng et al., 2013; Johari & Shenoy, 2012; F. Zeng, Zhang, & Tang, 2015). The calculated effective mass for WS_2, Janus WSSe, and WSe_2 monolayers are $0.57m_o$, $0.54m_o$, and $0.47m_o$ (m_o – effective mass of electron), respectively, and the corresponding mobility values are 0.02, 0.062, and 0.072 $m^2V^{-1}s^{-1}$. The partial density of states (PDOS) for WS_2, WSSe, and WSe_2 are shown in Fig 4.4. The valence band maximum (VBM) of WS_2 is mainly composed by W-d_{z2} and W-d_{zx} orbits, while conduction band minimum (CBM) is composed of W-d_{z2} mainly with a small contribution from W-d_{z2-y2} orbits. In WS_2 monolayer, the S-$3p_z$, S-$3p_x$, and W-d_{zx} orbitals contribute far from the Fermi level. In addition, the deeper energy levels in the CB are mainly attributed to the S-$3p_x$, W-d_{zx}, and S-$3p_z$ orbitals. The CBM of WSSe is contributed by W-d_{z2} and a small contribution from W-d_{x2-y2} orbitals while Se-px, W-d_{zx}, and W-d_{Z2} orbitals occupy the deeper region. The VBM is formed by W-d_{x2-y2}

and d_{z2}orbits, whereas S-3p_z, Se-p_x, S-p_x and Se-p_z orbitals occupy deeper energy levels, Figure 4.4 (d). The similar results observed for WSe_2 monolayer, shown in Figure 4.4 (f). The SOC included band structure is shown in Figure 4.5. The spin splitting observed is 0.43eV, 0.44eV, and 0.48eV for WS_2, WSSe, and WSe_2 monolayers, respectively. The observed SOC effect in band structure is in accordance with the previous reports (Amin et al., 2014; Soni & Jha, 2015).

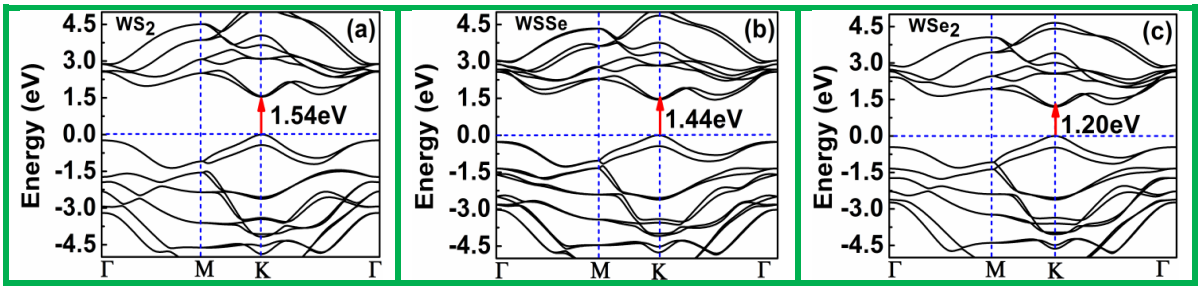

Figure 4.5 Band structures of (a) WS_2, (b) WSSe, and (c) WSe_2 monolayers using GGA-PBE+SOC

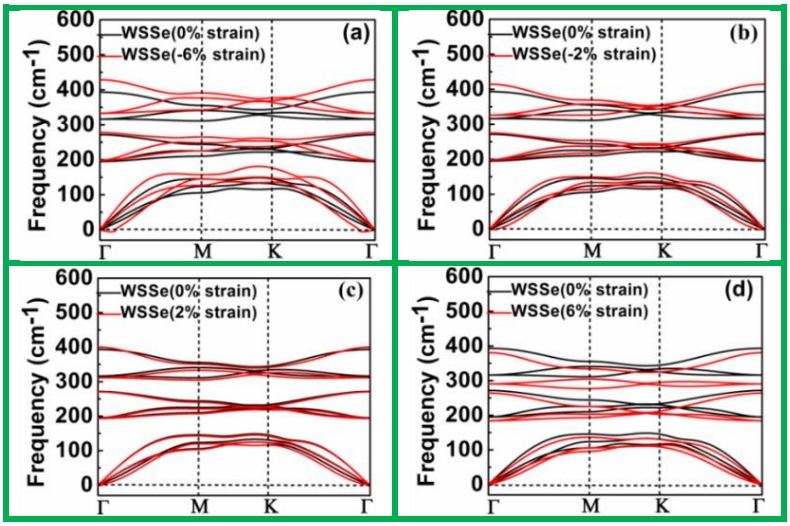

Figure 4.6 Phonon band dispersion (a) 6% compressive strain (b) 2% compressive strain (c) 2% tensile strain and (d) 6% tensile strain for WSSe monolayer

4.3.3 Strain effect on structural stability

Biaxial compressive (-8% to 0) and tensile (0 to + 8%) strains are employed to the considered monolayers to investigate the effect on their stability and electronic performance. The phonon band dispersion may help to find the maximum strain which can be sustain without breaking the symmetry. These results will help experimentalists to get the idea about choosing a suitable substrate. In addition, we also find the critical points where it breaks the original symmetry. Figure 4.6 shows the phonon band structure of WSSe monolayer at 2% and 6% compressive and tensile strains. These monolayers show the dynamic stability against tensile strain while thermodynamic instability occurs even at 2% under compressive strain. Under the tensile strain, acoustic modes (TA/LA) are softened and moved to a lower frequency. The bond length also increases with strain, which results in a weaker interaction between the atoms, thus reducing the frequency of the in-plane acoustic mode. The phonon mode, ZA has almost linear relationship with wave vector K. This is attributed to the decrease in the symmetry of the ZA mode against tensile strain (Aierken, Çakir, & Peeters, 2016). The optical modes also show that frequency reduction with increasing the tensile strain, which reduces the optical bandgap. Janus WSSe monolayer shows the optical modes softening in the order of in E′> A_2′′>E′′> A_1′. The IR and R modes of WSSe show higher sensitivity over WS_2 monolayer, but the optical R and IR modes are highly sensitive in WSSe monolayer under tensile strain.

The compressive strain reduced the bond length of monolayers, thereby distorting the crystal structure. This distortion along z-axis can cause structural instability. This can be confirmed by introducing an imaginary frequency under compressive strain for WSSe monolayer, shown in Figure 4.6 (a&b). The ZA acoustic mode shows the negative frequency at 2% compressive strain. Unlike WS_2 and WSSe, the WSe_2 monolayer appears to be more stable under compressive strain, with negative frequencies starting above 2% of compressive strain. Optical modes show stiffness under compressive strain because of enhancement in the force due to the reduced bond length. The order of the stiffness of phonon modes under the compressive strain is A_2''> E′> A_1'> E″ for the considered monolayers. The above strain-dependent phonon study suggests that the considered monolayers show thermodynamic instability around 2% or higher compressive strain and while they are more robust for tensile strain and can sustain more than 8% tensile strain. The detailed discussion of strain modulated phonon modes of WS_2 and WSe_2 monolayers are reported by Dixit and coworkers (Chaurasiya, Dixit, & Pandey, 2018a).

4.3.4 Strain effect on electronic properties

Electronic properties of considered monolayers are computed against compressive and tensile strains. The enhancement in the bandgap of WS_2 and WSe_2 monolayer are observed up to 1% compressive strain, which starts decreasing with increasing compressive strain further, Figure 4.8(a). Moreover, the WSSe monolayer follows the reduction in bandgap after 0.5% compression. The electronic transition like direct to indirect bandgap against compressive and tensile strain for monolayers is shown in Figure 4.7. The direct (K to K) to indirect transition (K to mid of K- Γ) is observed at 1.5%, 1%, and 1.5% compressive strains for WS_2, WSSe and WSe_2 monolayers, respectively. However, in the tensile strains at 0.5%, 1% and 2.5% strain electronic bandgap switch from direct (K to K) to indirect bandgap (K to Γ) for WS_2, WSSe and WSe_2 monolayers, respectively. The similar electronic transition for WS_2 and WSe_2 monolayer are reported by Udo and coworkers (Amin et al., 2014). The rate of reduction in bandgap of monolayers is more against tensile strain compared to compressive strain.

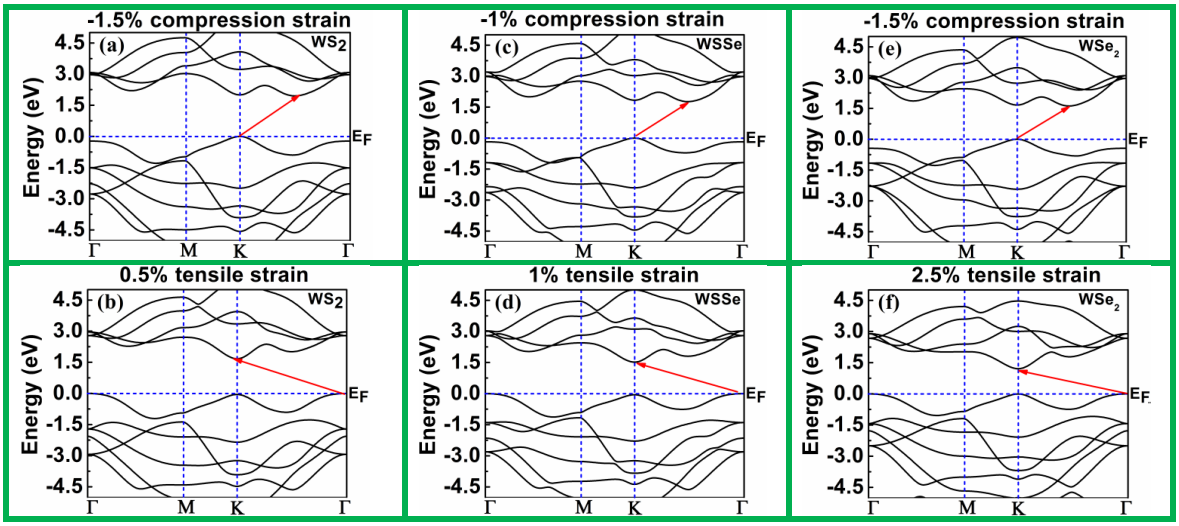

Figure 4.7 Electronic band structures of (a) and (b) at -1.5% compression strain and 0.5% tensile strain, respectively; (c) and (d) -1 % compression strain and 1% tensile strain, WSSe monolayer, respectively; (e) and (f)at -1.5% compression strain at 2.5% tensile strain, WSe2 monolayer, respectively.

In tensile strain, the X atoms stay away from W atom, resulting in a reduction of the bond angle X-W-X, which enhances the coupling between the chalcogen p and W-d_{z2} orbital and decreases the same chalcogen p and W-d_{x2-y2} orbitals. The change in hybridization induces the decrease in bandgap across E_K-E_Γ and also improves the bandgap across E_Σ-E_K. The energy bands in the VB

at Γ point shifted to Fermi energy compare to the energy band at K point under biaxial strain. The shifting in the band edge causes the change in direct to indirect bandgap against strain. Figure 4.7 shows the band structure of all considered monolayers and shows the direct (E_K-E_K) to indirect bandgap transition (E_Γ-E_K). The PDOS of each monolayer ensure that the CBM and VBM are influenced by W-d_{z2} orbitals. The compressive strain shows the reduction in W-X bond length and improvement in the X-W-X angle, which improves the coupling among chalcogen p and d_{x2-y2} orbitals and reduces among chalcogen p and W-d_{z2} orbitals. This is confirmed through the influence of PDOS in the CBM and VBM are contributed by the W-d_{z2} against the tensile strain. However, the W-d_{x2-y2} orbital is participating in the VBM and CBM against compressive strain. Figure 4.8(b) and Figure 4.8(c) show the variation of effective mass and mobility under strain. The change in the effective mass follows the similar trend like the bandgap against strain. The rate of change of effective mass is more across the tensile strain compare to compressive strain. The similar trends also followed in bandgap under strain, Figure 4.8 (a). The mobility of monolayers is calculated through the equation $\mu = \frac{e\tau}{m_{eff}}$; which is mainly affected via optical phonon scattering. The effect on the mobility of monolayers is plotted in Figure 4.8 (c), showing that mobility is almost unaffected under the compressive strain and change across the tensile strain. The mobility is increasing with tensile strain. The maximum mobility values are 0.41 $m^2V^{-1}s^{-1}$, 0.36 $m^2V^{-1}s^{-1}$ and 0.29 $m^2V^{-1}s^{-1}$ for WS_2, WSSe and WSe_2 monolayers, respectively at 8% tensile strain.

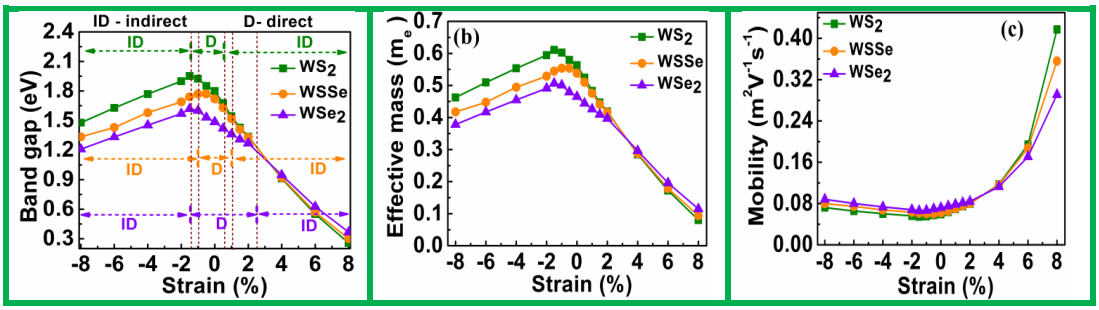

Figure 4.8 (a) Band gap, (b) effective mass and (c) mobility variation of WS2, WSSe and WSe2 monolayers (D and ID signify the Direct and Indirect band gap, respectively)

4.4 Conclusion

In this chapter, we studied the structural and electronic properties of WS_2, WSSe, and WSe_2 monolayer. The band structures of considered monolayers show the direct band gap. Janus WSSe monolayer shows the higher bandgap than the Janus MoSSe monolayer, and lies between that of WS_2 and WSe_2 monolayers. Dynamic stability of unstrained and strained monolayer is predicted using phonon band dispersion. All the considered monolayers are thermodynamically stable and can sustain 8% tensile strain and up to 1% compressive strain. The electronic transitions are investigated in biaxial compressive and tensile strained monolayers. The other electronic properties, like effective mass and mobility, are also studied for strained monolayers.